Above-threshold ionization by few-cycle Bessel pulses carrying orbital angular momentum

Birger Böning,[1,*] Willi Paufler,[1] and Stephan Fritzsche[1,2]
[1]*Theoretisch-Physikalisches Institut, Friedrich-Schiller-Universität Jena, D-07743 Jena, Germany*
[2]*Helmholtz-Institut Jena, D-07743 Jena, Germany*

(Received 26 April 2018; published 13 August 2018)

We investigate theoretically the above-threshold ionization (ATI) of localized atomic targets by intense few-cycle Bessel pulses that carry orbital angular momentum (OAM), known also as twisted light. More specifically, we use the strong-field approximation (SFA) to compute the photoelectron energy spectra. While for plane-wave laser pulses the outgoing photoelectron is typically described by Volkov states within the SFA, no equivalent is known for an electron in a twisted laser field. Here, we therefore introduce a local dipole approximation for the (continuum) state of the photoelectron that is justified for few-cycle pulses. Based on this approximation, we demonstrate that the photoelectrons can also be emitted into the propagation direction of the pulse. When measured in propagation direction, moreover, we show that the magnitude of the ATI peaks depend on the opening angle and the (projection of) total angular momentum of the Bessel pulse.

DOI: 10.1103/PhysRevA.98.023407

I. INTRODUCTION

Strong laser fields have been found to be a valuable tool to study electron dynamics in atoms and molecules. Various characteristic nonperturbative phenomena can be observed in the spectra of emitted photoelectrons and photons. In the above-threshold ionization (ATI), in particular, the photoelectron can absorb *more* photons than required in order to overcome the ionization threshold. The observed energy spectrum then consists of several peaks spaced by the photon energy [1,2]. In the past decades, the ATI of atoms by plane-wave femtosecond laser pulses has been extensively studied, both experimentally and theoretically. For instance, it was found that the duration and carrier envelope phase of the ionizing pulse sensitively influence the shape and symmetry of the resulting photoelectron momentum distributions [3,4]. More recently, in addition, complex pulse shapes, such as bicircular pulses, have been studied as well [5,6].

Several methods exist today to analyze theoretically the ATI. Perhaps the most exact approach is the direct numerical solution of the time-dependent Schrödinger equation, which often reproduces all experimental features of ATI. However, this approach is time consuming and quickly becomes unfeasible if atoms with more than a few (active) electrons are considered. Quite in contrast with numerically solving the Schrödinger equation, an analytical approach has been developed, which is known as the strong-field approximation (SFA) [7–9]. In its most rigorous form, the SFA neglects the interaction of the photoelectron with the parent ion as well as the laser-field dressing of the bound state. Based on these approximations, most features of ATI spectra can be reproduced qualitatively [2]. However, typical SFA-based studies also neglect nondipole contributions in the laser-atom interaction. This is justified especially for plane-wave laser fields, where relativistic and magnetic effects do not play a role.

Most nonlinear atomic processes can also be driven by laser beams with a more complex phase structure. In particular, twisted Bessel beams exhibit helical phase fronts that can experimentally be created using axicons [10], phase plates [11], or computer-generated holograms [12]. In contrast with plane waves, such twisted beams carry an often well-defined (projection of) orbital angular momentum (OAM) in addition to their spin angular momentum. In the past, for example, it was investigated how the OAM of the beam modifies the photoionization and excitation of atoms with twisted laser beams of low intensity [13–15]. These studies showed that OAM can be transferred to the electron, which modifies the selection rules when compared with the plane-wave case [16].

In the nonperturbative regime, twisted laser pulses of finite duration have been of interest in high-harmonic generation [17,18] as well as in two-color ionization processes [19,20]. In the former, it was shown that OAM is transferred from the fundamental to the high-harmonic modes, which enables one to create twisted pulses of attosecond duration. Less attention has been paid, in contrast, to the strong-field ionization of atoms using twisted laser pulses of high intensity. Only recently we applied a semiclassical approach to study the symmetries of photoelectron momentum distributions [21]. In a fully quantum-mechanical description of this strong-field ionization, it can be expected that the transfer of OAM to the photoelectron leads to significantly altered ATI peak structures and their study might provide new insights into the underlying laser-atom interaction. However, to make use of the SFA formalism, it needs to be extended beyond the dipole approximation in order to incorporate the helical phase structure of the ionizing pulse. More precisely, a proper description of the continuum states available to the photoelectron in a strong twisted pulse is needed.

In this work, we take a first step towards the quantum-mechanical description of ATI by strong few-cycle Bessel

*birger.boening@uni-jena.de

pulses. To this end, we introduce a local dipole approximation within the SFA in order to describe the continuum dressed by the twisted laser pulse. In this approximation, the wave function of the outgoing photoelectron is still based on the well-known nonrelativistic Volkov states and we use them to compute energy- and angle-differential photoelectron spectra. In these spectra, we clearly find photoelectrons emitted also along the propagation direction of the pulse, i.e., away from the usual emission *within* the x-y plane. Below, we analyze in detail how these energy spectra of the photoelectrons arise if the opening angle of the Bessel pulse is increased. Furthermore, we show that the ATI peaks observed in these spectra depend on the opening angle as well as the total angular momentum (TAM) of the Bessel pulse.

This paper is structured as follows: In Sec. II, the theoretical methods are discussed. We first introduce Bessel beams and finite Bessel pulses in Sec. II A and shortly review the SFA approach to ATI in Sec. II B. In Sec. II C, we then introduce the local dipole approximation and calculate the continuum states of the photoelectron in a strong Bessel pulse. With the resulting SFA transition amplitude, detailed calculations of the photoelectron energy spectra are performed in Sec. III. After reviewing the plane-wave limit, emphasis is placed especially on the dependence of the photoelectron spectra on the TAM and the opening angle of the Bessel pulse. Finally, a summary and outlook are given in Sec. IV.

Note that atomic units ($m_e = e = \hbar = 4\pi\varepsilon_0 = 1$) are used throughout the paper unless stated otherwise.

II. THEORETICAL METHODS

Figure 1 shows the geometry of the strong-field ionization as considered in this work. A few-cycle Bessel pulse of duration T and wavelength λ propagates along the z axis and interacts with a single atomic target that is displaced by an impact parameter $\boldsymbol{b} = (b, \varphi_b, z_b = 0)$ with regard to the beam axis, taken as the quantization axis. The photoelectrons emitted from the target are measured at the detector with asymptotic momentum $\boldsymbol{p} = (p, \vartheta_p, \varphi_p)$, parametrized in spherical coordinates. Below, we describe the bound state of the *single active electron* with binding energy $E_B = 14$ eV, as found, e.g., for krypton. To realize a strong-field regime as appropriate for the SFA, we assume a (central) wavelength $\lambda = 800$ nm and a pulse intensity $I = 10^{14}$ W/cm^2 (cf. Sec. II A for the definition of the intensity).

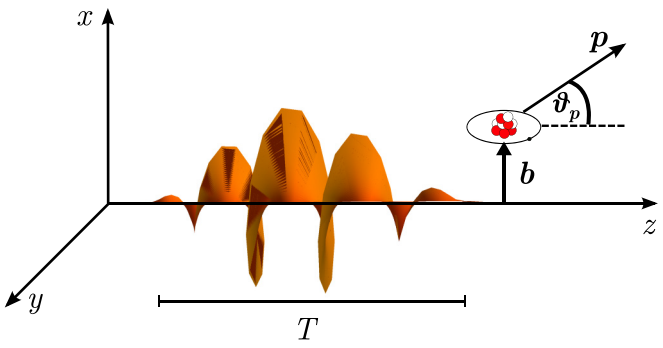

FIG. 1. Strong-field ionization of an atom by a few-cycle Bessel pulse (orange). The atomic target is localized at the impact parameter $\boldsymbol{b}$ relative to the beam z axis. The photoelectrons are observed with asymptotic momentum $\boldsymbol{p}$ at the detector.

A. Bessel pulses

Bessel pulses of finite duration can be formed from continuous Bessel beams, which are described by the vector potential $\boldsymbol{A}_{m\Lambda\vartheta_k}(\boldsymbol{r}, t)$ in the Coulomb gauge. These continuous Bessel beams are characterized by their frequency ω, helicity Λ, the (cone) opening angle ϑ_k, and the projection m of TAM onto their beam axis. Their vector potential is a solution to the wave equation

$$\left(\triangle - \alpha^2 \frac{\partial^2}{\partial t^2}\right) \boldsymbol{A}_{m\Lambda\vartheta_k}(\boldsymbol{r}, t) = 0 \tag{1}$$

and also satisfies the eigenvalue equation

$$\hat{J}_z \boldsymbol{A}_{m\Lambda\vartheta_k}(\boldsymbol{r}, t) = m \boldsymbol{A}_{m\Lambda\vartheta_k}(\boldsymbol{r}, t). \tag{2}$$

Here, $\hat{J}_z = \hat{L}_z + \hat{S}_z$ is the operator of TAM projection with the operators $\hat{L}_z$ of OAM projection and $\hat{S}_z$ of spin projection.

We can conveniently write down the solutions of Eqs. (1) and (2) if we introduce the eigenvectors $\boldsymbol{\eta}_{m_s}$ ($m_s = 0, \pm 1$) of the spin projection operator $\hat{S}_z$:

$$\hat{S}_z \boldsymbol{\eta}_{m_s} = m_s \boldsymbol{\eta}_{m_s}, \quad \boldsymbol{\eta}_0 = \begin{pmatrix} 0 \\ 0 \\ 1 \end{pmatrix}, \quad \boldsymbol{\eta}_{\pm 1} = \frac{\mp 1}{\sqrt{2}} \begin{pmatrix} 1 \\ \pm i \\ 0 \end{pmatrix}.$$

In this basis for the spin of the incident photons, the vector potential of a Bessel beam has the form

$$\boldsymbol{A}_{m\Lambda\vartheta_k}(\boldsymbol{r}, t) = e^{-i\omega t} \sum_{m_s = 0, \pm 1} \boldsymbol{\eta}_{m_s} A^{\mathrm{tw}}_{m_s}(\boldsymbol{r}), \tag{3}$$

with the expansion coefficients

$$A^{(\mathrm{tw})}_{m_s}(\boldsymbol{r}) = \sqrt{\frac{\varkappa}{2\pi}} (-i)^{m_s} c_{m_s} J_{m-m_s}(\varkappa r) e^{i(m-m_s)\varphi_r} e^{ik_z z}.$$

Here $\boldsymbol{r} = (r, \varphi_r, z)$ is the position vector in cylindrical coordinates, $J_{m-m_s}(\varkappa r)$ is a Bessel function of the first kind, and

$$c_{\pm 1} = \frac{1}{2}(1 \pm \Lambda \cos\vartheta_k), \quad c_0 = \frac{\Lambda}{\sqrt{2}} \sin\vartheta_k. \tag{4}$$

Note that the above solutions do not possess a definite OAM, although they have a well-defined TAM due to Eq. (2). In the following, we will therefore use the TAM projection m to characterize the angular-momentum properties of the Bessel beams.

To generate Bessel pulses $\boldsymbol{A}^P(\boldsymbol{r}, t)$ of finite duration, we need to multiply the vector potential (3) by the envelope

$$f(t) = \begin{cases} A_0 \sin^2\left(\frac{\omega t}{2n_p}\right), & 0 \leqslant t \leqslant T \\ 0 & \text{otherwise,} \end{cases}$$

where $T = n_p 2\pi/\omega$ denotes the duration of the pulse and n_p is the number of optical cycles. Note that one could also create a pulse as a weighted superposition of Bessel beams (3) in frequency space, which yields an *X wave* vector potential [22]. To obtain a simple model for a Bessel pulse, however, we only multiply by a temporal envelope. Our procedure gives

rise to a complex-valued expression for the vector potential of the Bessel pulse. However, since our goal is to describe nonlinear interactions with these pulses, we construct a real-valued vector potential by taking the imaginary part of Eq. (3). In line with previous works [21,23], we obtain the Cartesian components of the vector potential:

$$A_x^{(\mathrm{P})}(\boldsymbol{r},t) = f(t)\sqrt{\frac{\varkappa}{4\pi}}\{c_{-1}J_{m+1}(\varkappa r)\cos[(m+1)\varphi_r + k_z z - \omega t] + c_{+1}J_{m-1}(\varkappa r)\cos[(m-1)\varphi_r + k_z z - \omega t]\}, \tag{5a}$$

$$A_y^{(\mathrm{P})}(\boldsymbol{r},t) = f(t)\sqrt{\frac{\varkappa}{4\pi}}\{c_{-1}J_{m+1}(\varkappa r)\sin[(m+1)\varphi_r + k_z z - \omega t] - c_{+1}J_{m-1}(\varkappa r)\sin[(m-1)\varphi_r + k_z z - \omega t]\}, \tag{5b}$$

$$A_z^{(\mathrm{P})}(\boldsymbol{r},t) = f(t)\sqrt{\frac{\varkappa}{2\pi}}c_0 J_m(\varkappa r)\sin(m\varphi_r + k_z z - \omega t), \tag{5c}$$

which we shall use to analyze the strong-field ionization with Bessel pulses below. Since the vector potential (5) is given in the Coulomb gauge, the corresponding electric and magnetic fields are also real valued.

Perhaps most important for the strong-field regime is the *intensity* of the laser field. This intensity needs to be defined unambiguously, especially if we want to compare the ionization probabilities for laser fields of different (spatial) structure. In general, the intensity of a laser field is defined as the cycle-averaged Poynting vector. For an elliptically polarized plane-wave laser field of the form $\boldsymbol{A}(t) = A_0(1+\varepsilon^2)^{-1/2}[\cos(\omega t)\boldsymbol{e}_x + \varepsilon\sin(\omega t)\boldsymbol{e}_y]$ with the ellipticity $0 \leqslant \varepsilon \leqslant 1$, the Poynting vector only has a z component. The intensity of such a beam is therefore a direct measure of the energy flow in the propagation direction of the beam and is given by $I = A_0^2\omega^2/8\pi\alpha = E_0^2/8\pi\alpha$. For a Bessel pulse, in contrast, the Poynting vector has another component in the azimuthal direction and depends, in addition, on the transverse radial coordinate r. Following Ref. [24], we here define the intensity via the longitudinal component of the Poynting vector in the limit of long pulse duration, given by

$$I_\perp(r) = \frac{A_0^2\omega^2\varkappa}{4\pi}\left|c_{+1}^2 J_{m-1}^2(\varkappa r) - c_{-1}^2 J_{m+1}^2(\varkappa r)\right|. \tag{6}$$

Figure 2 displays a characteristic intensity profile of a Bessel beam that exhibits a ring-like structure in the transverse plane owing to the Bessel functions in Eq. (6). Of course, the intensity of a finite pulse will be also time dependent but with the intensity I of such a pulse, we shall always refer to the maximum value in expression (6).

We end this section by reviewing the parameters that define a Bessel pulse. Its temporal shape is determined by the central frequency $\omega = 2\pi c/\lambda$ and the pulse duration in terms of the number of optical cycles n_p. Its spatial properties are controlled by the helicity Λ, the TAM projection m, and the cone opening angle ϑ_k. Furthermore, we use the amplitude A_0 to specify the intensity according to Eq. (6).

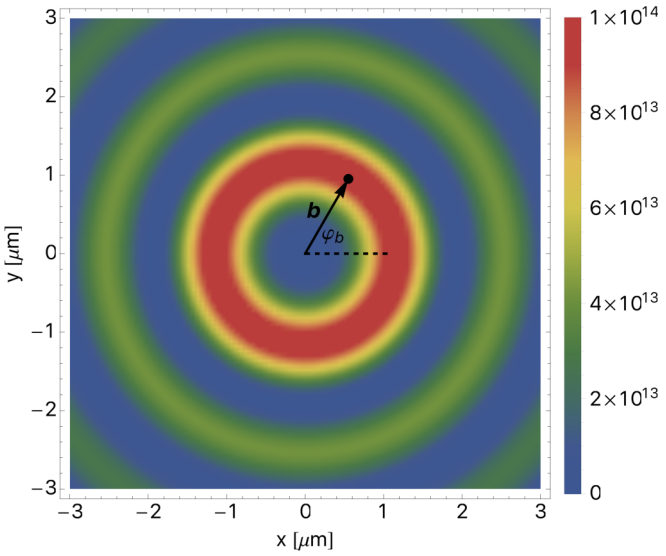

FIG. 2. Intensity profile $I_\perp(r)$ (in W/cm^2) of a Bessel pulse in the plane perpendicular to the propagation direction. The profile is shown for a pulse with $\lambda = 800$ nm, $\vartheta_k = 20^\circ$, $\Lambda = +1$, $m = 3$, and $I = I_\perp^{(\max)} = 10^{14}$ W/cm^2. We also indicate the impact parameter $\boldsymbol{b}$ of the atomic target.

Due to the fixed opening angle, Bessel pulses possess definite longitudinal ($\varkappa$) and transverse (k_z) components of linear momentum, respectively. Since the direction of the vector potential (5) strongly depends on the longitudinal component $\varkappa$, we expect that the opening angle has a significant influence on the ATI spectra.

B. Strong-field-approximation transition amplitude

Our aim is to analyze the angle-differential photoionization probability $\mathbb{P}(\boldsymbol{p})$ as a function of the asymptotic momentum $\boldsymbol{p}$ of the photoelectron (detector) for an atom that is ionized by a strong Bessel pulse of the form (5). Following Ref. [4], the probability for the emission of a photoelectron with energy $\boldsymbol{p}^2/2$ into the solid angle element $d\Omega_{\boldsymbol{p}}$ can be expressed in terms of a transition amplitude $T(\boldsymbol{p})$ via

$$\mathbb{P}_{\boldsymbol{b}}(\boldsymbol{p}) = p|T_{\boldsymbol{b}}(\boldsymbol{p})|^2, \tag{7}$$

with $p = |\boldsymbol{p}|$ and the energy $E = p^2/2$ of the photoelectron. Below, we refer to the energy dependence $\mathbb{P} = \mathbb{P}(E)$ of the angle-differential photoionization probability as the ATI *spectrum*, which parametrically depends also on the polar and azimuthal angles ϑ_p and φ_p as well as the impact parameter $\boldsymbol{b}$.

To derive an expression for the transition amplitude $T_{\boldsymbol{b}}(\boldsymbol{p})$ within the framework of the SFA, a further approximation is necessary to describe the emitted photoelectron in the Bessel pulse. We apply here a local dipole approximation, which is described in the next section. In general, the interaction of an atom with a laser field is described in velocity gauge by the Hamiltonian

$$\hat{H} = \hat{H}_0 + \hat{V}(\boldsymbol{r}) + \hat{V}_L(\boldsymbol{r},t), \tag{8}$$

where $\hat{H}_0 = \boldsymbol{p}^2/2$, $\hat{V}(\boldsymbol{r}) = -Z/r = -\sqrt{2E_B}/r$ is the Coulomb potential, and $\hat{V}_L(\boldsymbol{r},t) = \hat{\boldsymbol{p}}\boldsymbol{A}(\boldsymbol{r},t) + \boldsymbol{A}^2(\boldsymbol{r},t)$ describes the laser-electron interaction. Here, $\boldsymbol{A}(\boldsymbol{r},t)$ is the

vector potential of the laser field, which generally depends on position $\boldsymbol{r}$. This spatial dependence is particularly important for the present analysis, since the TAM of a Bessel pulse leads to a spatially dependent intensity profile (see Sec. II A).

Making use of the Hamiltonian (8), the transition amplitude of the strong-field ionization can be written as

$$T_{\boldsymbol{b}}(\boldsymbol{p}) = -i \int_{-\infty}^{\infty} dt \langle \psi_{\mathbf{p}}^{(\mathrm{C})}(t) | \hat{V}_L(\mathbf{r}, t) | \psi_0(t) \rangle. \tag{9}$$

Here $|\psi_{\mathbf{p}}^{(\mathrm{C})}(t)\rangle$ are the continuum states available to the photoelectron and $|\psi_0(t)\rangle = e^{iE_B t}|\Phi_0\rangle$ is the initial bound state with binding energy $E_B > 0$. An integration by parts in Eq. (9) yields

$$T_{\boldsymbol{b}}(\boldsymbol{p}) = -\langle \psi_{\mathbf{p}}^{(\mathrm{C})}(t) | \psi_0(t) \rangle \big|_0^T - i \int_0^T dt \langle \psi_{\mathbf{p}}^{(\mathrm{C})}(t) | V(\boldsymbol{r}) | \psi_0(t) \rangle, \tag{10}$$

where we have used that the vector potential is nonzero only for $0 \leqslant t \leqslant T$. Within the SFA, two assumptions are typically made to further evaluate this amplitude: we assume that the laser field does not disturb the initial bound state and, hence, $|\Phi_0\rangle$ is an eigenstate of the atomic Hamiltonian $\hat{H}_A = \hat{H}_0 + \hat{V}_C(\boldsymbol{r})$; second, we neglect the influence of the Coulomb potential on the motion of the photoelectron in the continuum. Therefore, the continuum states $|\psi_{\mathbf{p}}^{(\mathrm{C})}(t)\rangle$ are solutions of the Schrödinger equation for a free electron in a laser field,

$$i \frac{\partial}{\partial t} |\psi_{\mathbf{p}}^{(\mathrm{C})}(t)\rangle = (\hat{H}_0 + \hat{V}_L(\boldsymbol{r}, t)) |\psi_{\mathbf{p}}^{(\mathrm{C})}(t)\rangle. \tag{11}$$

If the dipole approximation $\boldsymbol{A}(\boldsymbol{r}, t) \approx \boldsymbol{A}(t)$ for a plane-wave laser pulse is applied, the solutions to Eq. (11) in velocity gauge are the well-known Volkov states

$$|\psi_{\mathbf{p}}^{(\mathrm{C})}\rangle = |\psi_{\mathbf{p}}^{(V)}\rangle = e^{-iS_V(t)} |\boldsymbol{p}\rangle,$$

with the Volkov phase

$$S_V(t) = \frac{1}{2} \int^t dt' [\boldsymbol{p} + \boldsymbol{A}(t')]^2.$$

We already mentioned above that we choose to work in velocity gauge. As was shown by Becker *et al.* in Ref. [25], this choice in general yields wrong ATI spectra and the length gauge is preferable. However, this discrepancy is not present for a $1s$ initial state considered in this paper. Furthermore, the length gauge does not exist in the general case when the vector potential is $\boldsymbol{r}$ dependent. Future work on a SFA-based description of the ATI with Bessel beams without making use of the local dipole approximation cannot be conducted in the length gauge. Therefore, in our case, the use of the velocity gauge is justified and more convenient in order to compare with future work.

C. Local dipole approximation and evaluation of transition amplitude

To evaluate the transition amplitude (10) for an ionizing Bessel pulse, we need to obtain a representation of the continuum states $|\psi_{\mathbf{p}}^{(\mathrm{C})}(t)\rangle$ for the photoelectron. Until the present, however, no such solution has been known, if the electron moves in an $\boldsymbol{r}$-dependent laser field $\boldsymbol{A}(\boldsymbol{r}, t)$. Below, we argue instead that, for a sufficiently short (few-cycle) Bessel pulse, the spatial dependence of the field is *locally* negligible for the time evolution of the photoelectrons. This is readily seen if we consider a classical electron in a plane-wave laser pulse, which has an electric field $\boldsymbol{E}(t) = E_0 \sin^2(\frac{\omega t}{2n_p}) \cos(\omega t) \boldsymbol{e}_x$ for $0 \leqslant t \leqslant 2\pi n_p/\omega$ and $\boldsymbol{E}(t) = 0$ otherwise. For our reasoning, it is sufficient to assume a linear polarization. From the classical equations of motion, $d^2\boldsymbol{x}/dt^2 = -\boldsymbol{E}(t)$, we then find that the electron propagates during the pulse duration over a distance of about

$$\Delta x \approx n_p \lambda \left(3 \times 10^{-14} \sqrt{I[\mathrm{W/cm^2}]} \lambda[\mathrm{nm}] + \frac{v_0}{c} \right),$$

where λ is the laser wavelength and v_0 is the initial velocity of the electron. For typical values of $I = 10^{14}$ W/cm^2, $\lambda = 800$ nm and a rather high initial velocity of $v_0 = 1$ a.u., we find $\Delta x \approx n_p \times 6$ nm. From Fig. 2, in contrast, we see that characteristic intensity variations of the Bessel beam occur on length scales of hundreds of nanometers. To a good approximation, we can therefore neglect the spatial structure of the Bessel pulse for modeling the dynamics of the photoelectron as long as the pulse is sufficiently short.

With these arguments in mind, we take the vector potential at the location of the atom, i.e., the impact parameter $\boldsymbol{b}$, $\boldsymbol{A}(\boldsymbol{r}, t) \approx \boldsymbol{A}^P(\boldsymbol{b}, t)$, and refer to this as the *local dipole approximation*. In this approximation, we can describe the continuum by the usual Volkov states

$$|\psi_{\mathbf{p}}^{(\mathrm{C})}\rangle \approx |\psi_{\mathbf{p},\boldsymbol{b}}^{(V)}\rangle = e^{-iS_{V,\boldsymbol{b}}(t)} |\boldsymbol{p}\rangle, \tag{12}$$

where the Volkov phase is now given in terms of the local vector potential,

$$S_{V,\boldsymbol{b}}(t) = \frac{1}{2} \int^t dt' [\boldsymbol{p} + \boldsymbol{A}(\boldsymbol{b}, t')]^2. \tag{13}$$

Using the explicit form (5) of the vector potential of the Bessel pulse, the Volkov phase can be written as a Fourier series,

$$S_{V,\boldsymbol{b}}(t) = \beta t + \sum_{j=1}^{9} \gamma_j \cos\left(\varphi_j^{(c)} - \omega_j^{(c)} t\right) + \sum_{l=1}^{13} \sigma_l \sin\left(\varphi_l^{(s)} - \omega_l^{(s)} t\right). \tag{14}$$

In this expression, all the coefficients $\beta, \gamma_j, \sigma_l$, the frequencies $\omega_j^{(c)}$, $\omega_l^{(s)}$, as well as the phases $\varphi_j^{(c)}$, $\varphi_l^{(s)}$ depend on the laser parameters A_0, n_p, ω, Λ, m, ϑ_k, the impact parameter $\boldsymbol{b}$, and the photoelectron momentum $\boldsymbol{p}$. Explicit expressions of these quantities are given in Appendix A. Physically, $\omega_j^{(c)}$ and $\omega_l^{(s)}$ describe the frequencies of the quiver motion of the photoelectron in the field of the Bessel pulse.

We are now prepared to make use of the continuum states (12) to further evaluate the transition amplitude (10) and to recast it into a useful form,

$$T_{\boldsymbol{b}}(\boldsymbol{p}) \approx -\langle \boldsymbol{p} | \Phi_0 \rangle \, e^{i[S_{V,\boldsymbol{b}}(t) + E_B t]} \big|_0^T - i \langle \boldsymbol{p} | V(r) | \Phi_0 \rangle \times \int_0^T dt e^{i[S_{V,\boldsymbol{b}}(t) + E_B t]}. \tag{15}$$

For all further computations, we here assume a hydrogen-like $1s$ initial state with binding energy E_B,

$$\Phi_0(r) = \frac{(2E_B)^{3/4}}{\sqrt{\pi}} e^{-\sqrt{2E_B}r},$$

for which the Fourier transform and matrix element of $V(r)$ can readily be evaluated analytically,

$$\langle \boldsymbol{p}|\Phi_0\rangle = \frac{(2E_B)^{5/4}}{\pi\sqrt{2}} \frac{1}{\left(\frac{p^2}{2}+E_B\right)^2},$$

$$\langle \boldsymbol{p}|V(r)|\Phi_0\rangle = -\frac{2^{3/4}E_B^{5/4}}{\pi} \frac{1}{\frac{p^2}{2}+E_B}.$$

In fact, the main task in computing the transition amplitude (15) for given laser parameters and photoelectron momentum $\boldsymbol{p}$ now is the evaluation of $e^{iS_{V,\boldsymbol{b}}(t)}$ and its integral. These computations have been performed numerically based on expression (14).

III. RESULTS AND DISCUSSION

We now make use of our result (15) for the SFA transition amplitude in order to compute the angle- and energy-differential ionization probability (7) for the strong-field ionization of a single atom in a strong Bessel pulse and to analyze the resulting ATI spectra for different laser parameters. In particular, we here aim to understand how the TAM m and the opening angle ϑ_k affect the emission of the photoelectrons. In this section, we therefore fix the wavelength $\lambda = 800$ nm, the number of cycles $n_p = 2$, the maximum intensity $I = 10^{14}$ W/cm^2 and the helicity $\Lambda = +1$. Moreover, we assume a single target atom with binding energy $E_B = 14$ eV (for example, Kr). For each set of parameters m and ϑ_k, the target atom is placed at the impact parameter $\boldsymbol{b} = (b_{\max}, \varphi_b = 0, z = 0)$, where $b_{\max}$ is the respective radial coordinate of maximum intensity I of the pulse (cf. Fig. 2).

A. Plane-wave limit

We first consider the ATI spectra computed for the ionization by a Bessel pulse in the plane-wave limit. As discussed in detail in Ref. [13], the vector potential (3) coincides with a circularly polarized (in the x-y plane) plane wave of helicity Λ in the limit $\vartheta_k \ll 1$ and $m = \Lambda$. In this limit, the spin coefficients (4) are $c_j \to \delta_{j\Lambda}$ and the vector potential (5) of the Bessel pulse becomes

$$A_x^{(\mathrm{P})}(\boldsymbol{r},t) = \tilde{A}_0 \sin^2\left(\frac{\omega t}{2n_p}\right)\cos(\omega t - k_z z), \tag{16a}$$

$$A_y^{(\mathrm{P})}(\boldsymbol{r},t) = \Lambda\tilde{A}_0 \sin^2\left(\frac{\omega t}{2n_p}\right)\sin(\omega t - k_z z), \tag{16b}$$

$$A_z^{(\mathrm{P})}(\boldsymbol{r},t) = 0, \tag{16c}$$

where we defined $\tilde{A}_0 = A_0\sqrt{\frac{\varkappa}{4\pi}}$. Figure 3(c) shows this vector potential in the polarization plane as a function of time.

To compute the ATI spectra in the plane-wave limit, we use our general result for the transition amplitude (15) and the Volkov phase (14). We place the detector in the polarization plane ($\vartheta_p = \pi/2$) and vary the azimuthal angle φ_p. In Figs. 3(a) and 3(b) we show the resulting ATI spectra for detectors placed in opposite directions $\varphi_p = 0,\ \pi$ and $\varphi_p = \pi/2,\ 3\pi/2$, respectively. The characteristic ATI peaks can be observed for $\varphi_p = 0$. Furthermore, the dependence of the ATI spectra on the azimuthal angle may be directly compared with the SFA computations of Milošević *et al.* [4], who discussed asymmetries depending on the carrier envelope phase in the ATI spectra from few-cycle pulses. In our case, we can read off a carrier envelope phase of zero from the limiting vector potential (16). This leads to significantly different ATI spectra measured in the $\pm x$ direction [Fig. 3(a)] and identical ATI spectra in the $\pm y$ direction [Fig. 3(b)]. In addition, note that some ATI peaks are suppressed in Fig. 3. This results from the short duration of the ionizing pulse and the peaks would develop with increasing pulse length due to interferences from many optical cycles. These findings are identical to the results shown in Fig. 10 of Ref. [4].

In summary, our formalism yields correct differential ionization probabilities in the plane-wave limit and we can now turn to the general case of the ATI with a Bessel pulse.

B. Bessel pulse

The most characteristic property of the Bessel pulse vector potential (5) is its nonzero z component for nonvanishing opening angle ϑ_k and TAM m. This property has consequences for the ionization dynamics in strong fields: the classical

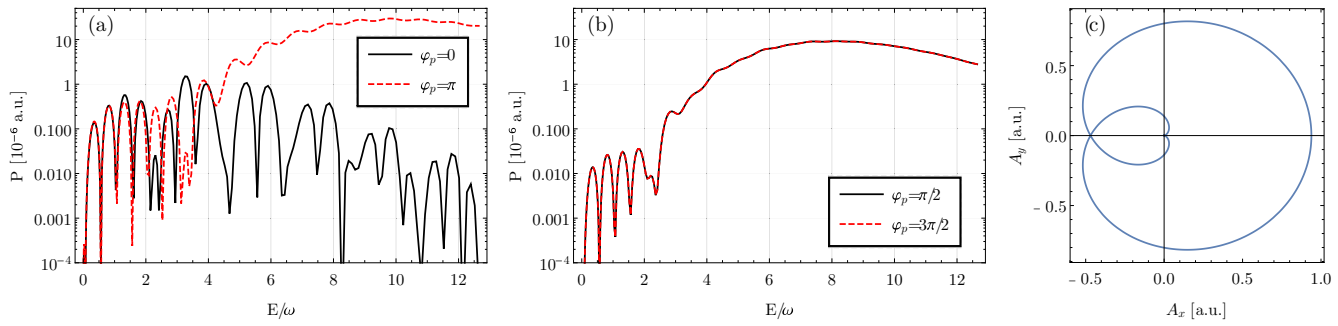

FIG. 3. ATI with an intense two-cycle Bessel pulse in the plane-wave limit with opening angle $\vartheta_k = 1^\circ$ and TAM $m = \Lambda = +1$. Calculated ATI spectra are shown for photoelectrons emitted in the polarization plane ($\vartheta_p = \pi/2$) in the (a) $\pm x$ directions ($\varphi_p = 0, \pi$) and (b) $\pm y$ directions ($\varphi_p = \pi/2, 3\pi/2$). The vector potential as a function of time is shown in panel (c). An intense Bessel pulse with $\lambda = 800$ nm and $I = 10^{14}$ W/cm^2 was applied for a target atom with binding energy of $E_B = 14$ eV.

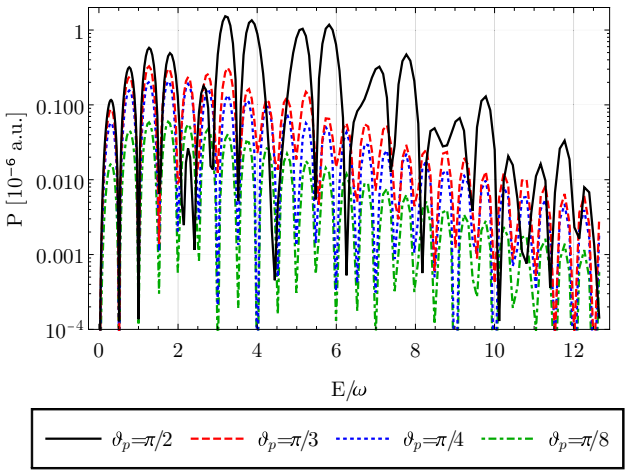

FIG. 4. ATI spectra computed for different polar emission angles ϑ_p and an azimuthal angle $\varphi_p = 0$. Results are shown for a Bessel pulse with TAM $m = 2$ and opening angle $\vartheta_k = 20^\circ$. In each case, the target atom was placed at impact parameter $\boldsymbol{b} = (b_{\max},\ \varphi_b = 0,\ z_b = 0)$, where $b_{\max}$ is the radial coordinate of maximum longitudinal intensity of the pulse. All other parameters are the same as in Fig. 3.

conservation of canonical momentum of the photoelectron reads

$$\boldsymbol{p}(t_0) - \boldsymbol{A}^{(\mathrm{P})}(\boldsymbol{b}, t_0) = \boldsymbol{p}(t \to \infty) - \boldsymbol{A}^{(\mathrm{P})}(\boldsymbol{b}, t \to \infty), \quad (17)$$

where t_0 is the time at which the electron is released from the atom into the continuum and $\boldsymbol{A}^{(\mathrm{P})}(t \to \infty) = 0$. Hence, we expect that the photoelectron gains a momentum component p_z parallel to the propagation direction of the ionizing laser pulse if $A_z^{(\mathrm{P})}(t_0) \neq 0$. Thereby, the magnitude of p_z is proportional to the $A_z^{(\mathrm{P})}$ component. We therefore expect that photoelectrons can be detected away from the x-y plane in the ATI, which would not be present in the plane-wave case. Motivated by this classical reasoning, we now analyze the ATI spectra of these photoelectrons using the SFA formalism.

In Fig. 4, we show the differential ionization probabilities for photoelectrons emitted at different polar angles ϑ_p, while the azimuthal angle $\varphi_p = 0$ was held constant. The results were obtained for a Bessel pulse with opening angle $\vartheta_k = 20^\circ$ and TAM $m = 2$, which gives rise to a significant magnitude of the $A_z^{(\mathrm{P})}$ component. The black, solid curve corresponds to the same detector placement as the black, solid curve in Fig. 3 and serves here as a reference for photoelectrons emitted at different polar angles. All curves in Fig. 4 show ATI peaks similar to those in the plane-wave limit above [cf. black curve in Fig. 3(a)], since the position of the ATI peaks is a result of the interference of all frequencies occurring in the Volkov phase (14). These frequencies are completely determined by the central frequency ω and the number of cycles n_p of the pulse and have no dependence on the spatial parameters of the Bessel pulse.

Most notably, Fig. 4 demonstrates that the nonvanishing opening angle of the Bessel pulse leads indeed to a measurable ionization probability in the forward direction. We can make this statement more precise by comparing the probability of emission in the x-y plane ($\vartheta_p = \pi/2$, green, dot-dashed in Fig. 4) with that of emission away from this plane. For $\vartheta_p = \pi/3$, we would measure about half the number of photoelectrons. About 10 percent can still be observed under an angle of $\vartheta_p = \pi/4$ and this fraction decreases further when the detector is placed more and more towards the propagation axis. This confirms our classical reasoning from above and also extends our previous semiclassical work [21], where no detailed analysis of ATI peaks was possible.

In the following, we analyze the dependence of the forward ATI spectra on the opening angle ϑ_k and the TAM m of the Bessel pulse. In Fig. 5, we show the probability of emission at a polar angle $\vartheta_p = \pi/8$. Note that, for better visibility, we use here a linear scale for the ionization probability in contrast with the logarithmic scale in the ATI spectra discussed above. In Fig. 5(a), the ATI spectra are shown as a function of the opening angle ϑ_k for fixed TAM $m = 2$. As discussed above, the probabilities of emission parallel to the z axis should increase with the magnitude of the $A_z^{(\mathrm{P})}$ component of the Bessel vector potential (5). Since $A_z^{(\mathrm{P})} \sim c_0 \sim \sin\vartheta_k$, we expect the magnitudes of ATI peaks measured away from the x-y plane to increase with the opening angle ϑ_k. This

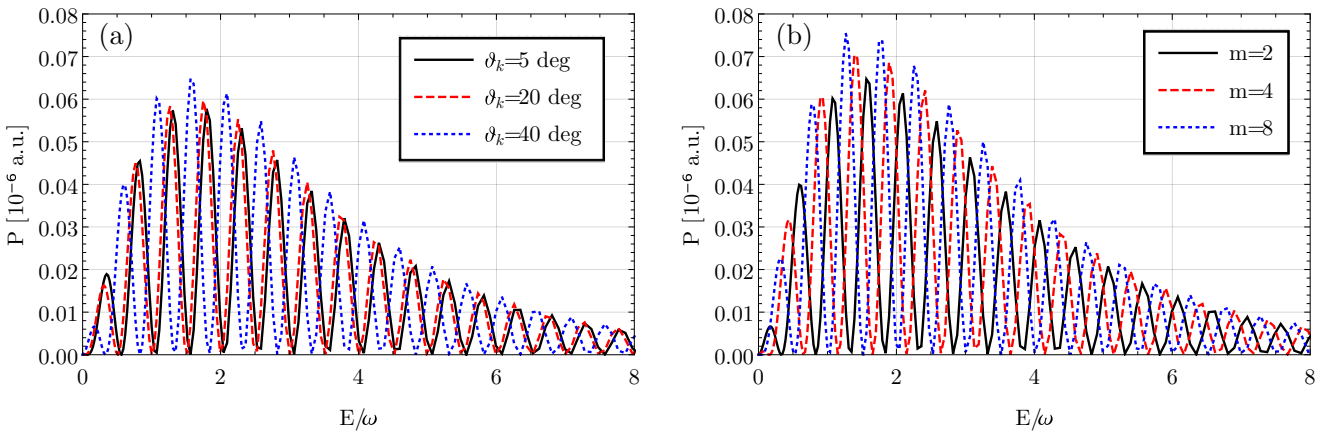

FIG. 5. ATI spectra for (a) different opening angles ϑ_k (left) with $m = 2$ and (b) different TAM m with $\vartheta_k = 20^\circ$ (right). Results are shown for photoelectrons emitted in $\vartheta_p = \pi/8$ and $\varphi_p = 0$. In each case, the target atom was placed at impact parameter $\boldsymbol{b} = (b_{\max},\ \varphi_b = 0,\ z_b = 0)$, where $b_{\max}$ is the radial coordinate of maximum longitudinal intensity of the pulse. All other parameters are the same as in Fig. 3.

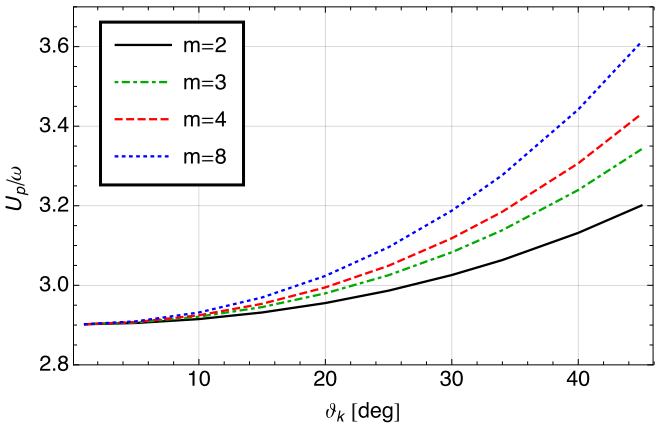

FIG. 6. Ponderomotive energy $U_p = \beta - p^2/2$ as a function of the opening angle ϑ_k for four values of the TAM m of the Bessel pulse. The pulse wavelength $\lambda = 800$ nm, longitudinal intensity $I = 10^{14}$ W/cm^2 and helicity $\Lambda = +1$ are fixed.

behavior can indeed be observed in Fig. 5(a): increasing the opening angle from $\vartheta_k = 5^\circ$ (black solid curve) to $\vartheta_k = 40^\circ$ (blue dotted curve) leads to an increase of about 10 percent in ionization probability in the dominant part of the spectrum. A similar behavior is found if the TAM m of the Bessel pulse is varied: Fig. 5(b) shows the dependence of the ATI spectra for $\vartheta_p = \pi/8$ computed for four different values of the TAM. The number of photoelectrons emitted in this direction is small compared with those observed perpendicular to the propagation direction of the pulse if $m = 2$. However, the magnitude of the ATI peaks can be considerably increased if the Bessel pulse carries a larger TAM.

Moreover, both Figs. 5(a) and 5(b) show a second effect: an increase of the opening angle or the TAM of the ionizing pulse imposes a constant shift of the spectrum towards lower energies. From a formal point of view, we can understand these shifts of the ATI spectra by looking at the Volkov phase (14). The relative positions and strengths of the ATI peaks are controlled by the frequencies $\omega_j^{(c)}$ and $\omega_j^{(s)}$ as well as the corresponding Fourier coefficients γ_j and σ_j. However, a constant shift of the spectrum is a result of a change in the coefficient β. To give this parameter a physical meaning, we write it in the form $\beta = \frac{p_z^2}{2} + U_p$, where

$$U_p = \tfrac{3}{32} A_0^2 \left(2\alpha_{-1}^2 + 2\alpha_1^2 + \alpha_0^2\right) \tag{18}$$

is the ponderomotive energy of the photoelectron in the Bessel pulse. In this expression, the coefficients α_j depend on the opening angle ϑ_k, the TAM m and the impact parameter b and are given in the appendix.

In Fig. 6, the ponderomotive energy is shown as function of ϑ_k for four values of the TAM. We see that U_p increases with the opening angle for all values of m. Also, higher values of m yield a higher ponderomotive energy for all ϑ_k and this difference is larger for larger opening angle. We therefore see that for the same *longitudinal* intensity, the opening angle and the TAM of the Bessel pulse determine U_p and accordingly yield a shift in the observed ATI spectra.

The results presented in this section demonstrate that the ATI with short Bessel pulses leads to significant ionization probabilities in forward direction, which depend on both the opening angle and the TAM of the Bessel pulse. In our discussion, we always set $\Lambda = 1$. However, all the effects presented above are also present for $\Lambda = -1$. Moreover, changes in the intensity, binding energy, or wavelength of the ionizing pulse do not significantly alter the ionization process as long as the SFA is valid. In particular, the dependencies on the opening angle of the ionizing pulse and on the polar angle investigated above do not change with intensity, since only the relative amplitudes of A_z to A_x are important for the emission angle of the photoelectron. However, the ponderomotive energy (18) changes proportional to the intensity, which would induce a shift in the ATI peaks. Similarly, the effect of a different binding energy or wavelength, respectively, is a shift of all ATI peaks due to energy conservation. However, we stress that the duration of the Bessel pulse has to be small in order to justify the local dipole approximation (cf. Sec. II C) and that the ATI spectra might look very different for long pulses.

IV. CONCLUSIONS

In this work, we investigated theoretically the strong-field ionization of single atoms with few-cycle Bessel pulses that carry nonzero OAM. Based on the SFA and a local dipole approximation, we showed that this property of the ionizing pulse leads to the emission of photoelectrons parallel to the propagation direction of the pulse ($p_z \neq 0$). Therefore, the strong-field ionization with Bessel pulses generates ATI peaks in forward direction. Moreover, we analyzed the dependence of the ATI spectra on the characterizing parameters of the ionizing pulse. We showed that the magnitude of the ATI peaks observed in forward direction are modified if the opening angle or the TAM of the pulse are changed.

In the future, this work can be extended to analyze atomic targets of finite size. It is an important question if dependencies on the TAM or the opening angle remain in the ATI when targets of finite size are considered. Furthermore, an investigation of the transfer of angular momentum from the strong Bessel pulse to the photoelectron promises interesting physical insight into the underlying processes. However, the local dipole approximation used in this work neglects any spatial effects in the photoelectron continuum and is therefore inappropriate in this regard. Future work should therefore also focus on a Volkov-like description of the continuum including nondipole effects.

ACKNOWLEDGMENT

The work reported in this paper was supported by the Priority Programme 1840 "Quantum Dynamics in Tailored Intense Fields" (QUTIF) of the German Research Foundation (DFG) under Contract No. FR 1251/17-1.

APPENDIX: VOLKOV PHASE

The Volkov phase (13) with $\boldsymbol{A}(\boldsymbol{b}, t) = \boldsymbol{A}^P(\boldsymbol{b}, t)$, where $\boldsymbol{A}^P(\boldsymbol{b}, t)$ is the vector potential (5) of the Bessel pulse, can be evaluated by performing a Fourier decomposition

of the integrand and then integrating the resulting sum of harmonic terms. The result is

$$S_{V,\boldsymbol{b}}(t) = \beta t + \sum_{j=1}^{9} \gamma_j \cos\left(\varphi_j^{(c)} - \omega_j^{(c)} t\right) + \sum_{l=1}^{13} \sigma_l \sin\left(\varphi_l^{(s)} - \omega_l^{(s)} t\right). \tag{A1}$$

with the frequencies and phases given by

$$\boldsymbol{\omega}^{(c)} = \omega\left(1, 1, 1, \frac{n_p-1}{n_p}, \frac{n_p-1}{n_p}, \frac{n_p-1}{n_p}, \frac{n_p+1}{n_p}, \frac{n_p+1}{n_p}, \frac{n_p+1}{n_p}\right), \tag{A2}$$

$$\boldsymbol{\omega}^{(s)} = \omega\left(-\frac{1}{n_p}, -\frac{2}{n_p}, 1, 2, 1, \frac{2n_p-1}{n_p}, \frac{n_p-1}{n_p}, 2\frac{n_p-1}{n_p}, \frac{n_p-1}{n_p}, 2\frac{n_p+1}{n_p}, \frac{n_p+1}{n_p}, \frac{n_p+1}{n_p}, \frac{2n_p+1}{n_p}\right), \tag{A3}$$

$$\boldsymbol{\varphi}^{(c)} = \varphi_b(m-1, m, m+1, m-1, m, m+1, m-1, m, m+1), \tag{A4}$$

$$\boldsymbol{\varphi}^{(s)} = \varphi_b(0, 0, m-1, 2m, m+1, 2m, m-1, 2m, m+1, 2m, m-1, m+1, 2m), \tag{A5}$$

and with the Fourier coefficients

$$\beta = \frac{p^2}{2} + \frac{3}{32} A_0^2 \left(2\alpha_{-1}^2 + 2\alpha_1^2 + \alpha_0^2\right), \tag{A6}$$

$$\boldsymbol{\gamma} = \frac{A_0}{2\omega}\left(-p_y\alpha_1, p_z\alpha_0, p_y\alpha_{-1}, \frac{n_p p_y \alpha_1}{2(n_p-1)}, -\frac{n_p p_z \alpha_0}{2(n_p-1)}, -\frac{n_p p_y \alpha_{-1}}{2(n_p-1)}, \frac{n_p p_y \alpha_1}{2(n_p+1)}, -\frac{n_p p_z \alpha_0}{2(n_p+1)}, -\frac{n_p p_y \alpha_{-1}}{2(n_p+1)}\right), \tag{A7}$$

$$\begin{aligned}\boldsymbol{\sigma} = \frac{A_0}{2\omega}\Bigg(&-\frac{A_0 n_p}{4}\left(2\alpha_1^2 + 2\alpha_{-1}^2 + \alpha_0^2\right), \frac{A_0 n_p}{32}\left(2\alpha_1^2 + 2\alpha_{-1}^2 + \alpha_0^2\right), -p_x\alpha_1, \frac{3A_0}{32}\left(\alpha_0^2 - 4\alpha_{-1}\alpha_1\right), \\ &-p_x\alpha_{-1}, \frac{A_0 n_p}{8(2n_p-1)}\left(4\alpha_{-1}\alpha_1 - \alpha_0^2\right), \frac{n_p p_x \alpha_1}{2(n_p-1)}, \frac{A_0 n_p}{64(n_p-1)}\left(\alpha_0^2 - 4\alpha_{-1}\alpha_1\right), \frac{n_p p_x \alpha_{-1}}{2(n_p-1)}, \\ &\frac{A_0 n_p}{64(n_p+1)}\left(\alpha_0^2 - 4\alpha_{-1}\alpha_1\right), \frac{n_p p_x \alpha_1}{2(n_p+1)}, \frac{n_p p_x \alpha_{-1}}{2(n_p+1)}, \frac{A_0 n_p}{8(2n_p+1)}\left(4\alpha_{-1}\alpha_1 - \alpha_0^2\right)\Bigg).\end{aligned} \tag{A8}$$

The factors α_j ($j = 0, \pm 1$) encode the spatial structure of the Bessel pulse and are defined as

$$\alpha_{-1} = \frac{1}{\sqrt{2}}\sqrt{\frac{\varkappa}{2\pi}} c_{-1} J_{m+1}(\varkappa b), \tag{A9a}$$

$$\alpha_0 = \sqrt{\frac{\varkappa}{2\pi}} c_0 J_m(\varkappa b), \tag{A9b}$$

$$\alpha_1 = \frac{1}{\sqrt{2}}\sqrt{\frac{\varkappa}{2\pi}} c_1 J_{m-1}(\varkappa b). \tag{A9c}$$

[1] P. Agostini, F. Fabre, G. Mainfray, G. Petite, and N. K. Rahman, Phys. Rev. Lett. **42**, 1127 (1979).

[2] W. Becker, F. Grasbon, R. Kopold, D. Milošević, G. Paulus, and H. Walther, in *Advances In Atomic, Molecular, and Optical Physics* (Elsevier, San Diego, 2002), pp. 35–98.

[3] G. G. Paulus, F. Lindner, H. Walther, A. Baltuška, E. Goulielmakis, M. Lezius, and F. Krausz, Phys. Rev. Lett. **91**, 253004 (2003).

[4] D. B. Milošević, G. G. Paulus, D. Bauer, and W. Becker, J. Phys. B: At. Mol. Opt. Phys. **39**, R203 (2006).

[5] D. B. Milošević and W. Becker, Phys. Rev. A **93**, 063418 (2016).

[6] C. A. Mancuso, D. D. Hickstein, K. M. Dorney, J. L. Ellis, E. Hasović, R. Knut, P. Grychtol, C. Gentry, M. Gopalakrishnan, D. Zusin, F. J. Dollar, X.-M. Tong, D. B. Milošević, W. Becker, H. C. Kapteyn, and M. M. Murnane, Phys. Rev. A **93**, 053406 (2016).

[7] L. V. Keldysh, Sov. Phys. JETP **20**, 1307 (1965).

[8] F. H. M. Faisal, J. Phys. B: At. Mol. Phys. **6**, L89 (1973).

[9] H. R. Reiss, Phys. Rev. A **22**, 1786 (1980).

[10] J. Arlt and K. Dholakia, Opt. Commun. **177**, 297 (2000).

[11] M. Beijersbergen, R. Coerwinkel, M. Kristensen, and J. Woerdman, Opt. Commun. **112**, 321 (1994).

[12] N. R. Heckenberg, R. McDuff, C. P. Smith, and A. G. White, Opt. Lett. **17**, 221 (1992).

[13] O. Matula, A. G. Hayrapetyan, V. G. Serbo, A. Surzhykov, and S. Fritzsche, J. Phys. B: At. Mol. Opt. Phys. **46**, 205002 (2013).

[14] H. M. Scholz-Marggraf, S. Fritzsche, V. G. Serbo, A. Afanasev, and A. Surzhykov, Phys. Rev. A **90**, 013425 (2014).

[15] A. A. Peshkov, D. Seipt, A. Surzhykov, and S. Fritzsche, Phys. Rev. A **96**, 023407 (2017).

[16] A. Picón, J. Mompart, J. R. V. de Aldana, L. Plaja, G. F. Calvo, and L. Roso, Opt. Express **18**, 3660 (2010).

[17] G. Gariepy, J. Leach, K. T. Kim, T. J. Hammond, E. Frumker, R. W. Boyd, and P. B. Corkum, Phys. Rev. Lett. **113**, 153901 (2014).

[18] D. Gauthier, P. R. Ribic, G. Adhikary, A. Camper, C. Chappuis, R. Cucini, L. F. DiMauro, G. Dovillaire, F. Frassetto, R. Géneaux, P. Miotti, L. Poletto, B. Ressel, C. Spezzani, M. Stupar, T. Ruchon, and G. De Ninno, Nat. Commun. **8**, 14971 (2017).

[19] D. Seipt, R. A. Müller, A. Surzhykov, and S. Fritzsche, Phys. Rev. A **94**, 053420 (2016).

[20] B. Böning, W. Paufler, and S. Fritzsche, Phys. Rev. A **96**, 043423 (2017).

[21] W. Paufler, B. Böning, and S. Fritzsche, Phys. Rev. A **97**, 043418 (2018).

[22] M. Ornigotti, C. Conti, and A. Szameit, Phys. Rev. Lett. **115**, 100401 (2015).

[23] G. F. Quinteiro, D. E. Reiter, and T. Kuhn, Phys. Rev. A **95**, 012106 (2017).

[24] A. Surzhykov, D. Seipt, and S. Fritzsche, Phys. Rev. A **94**, 033420 (2016).

[25] D. Bauer, D. B. Milošević, and W. Becker, Phys. Rev. A **72**, 023415 (2005).